Supplementary Information for:

Octave boxes inspired energy regularization triboelectric nanogenerator for high-efficient wave energy harvesting

Yuanchao Ren[1,2], Zizhuo Wang[1,2], Jie Chen[3,*], Fei Wu [1,*] and Hengyu Guo[1,2,*]

1 State Key Laboratory of Mechanical Transmission, College of Mechanical and Vehicle Engineering, Chongqing University, Chongqing, 400044, China

2 School of Physics, Chongqing University, Chongqing, 400044, China

3 College of Physics and Electronic Engineering, Chongqing Normal University, Chongqing 401331, China

*Correspondence: chenjie@cqnu.edu.cn (J. Chen), wufeifrank@cqu.edu.cn (F. Wu), physghy@cqu.edu.cn (H. Guo)

Content

Supplementary Table

Supplementary Note

Supplementary Figures

Figure S15. Photograph of the ER-TENG floating on the water.

Figure S16. Voltage curve of the thermohygrometer driven by ER-TENG with PMC. Inset is the work state.

Figure S17. (a) Top and (b) side view of the stator fixing medium materials. (c) Top view of electrode plate, the gap is clearly visible. (d) Side view of the PE passing through the gap of the electrode plate.

Figure S18. A photograph of the rotor, where the yellow area represents the 25 μm PA film and the milky white area represents the 10 μm PTFE film.

Figure S19. Top and side view of the stacked TENG. Scale bar is 2 cm.

Figure S20. Photograph of the mass (kg) of ER-TENG.

Supplementary Movies

Movie S1. Working process of ER-TENG.

Movie S2. The transmission relationship of gears demonstrated by SolidWorks.

Movie S3. Elastic flaps contact with the stopper ring.

Movie S4. Rotate speed comparison between with and without centrifugal speed limiter.

Movie S5. 944 LEDs are constantly lighted up by the ER-TENG.

Movie S6. Self-powered wind speed sensing based on the ER-TENG.

Movie S7. Nuclear radiation detector charged by the ER-TENG.

Movie S8. Self-powered thermohygrometer based on the ER-TENG.

Table S1. Gear set parameters for different transmission ratios

	1:1	2:1	3:1	4:1	6:1	8:1	10:1
A	M1.5 Z38	M1.5 Z38	M1.5 Z38	M1.5 Z38	M1.5 Z38	M1.5 Z38	M1.5 Z38
B	M1.5 Z30	M1.5 Z30	M1.5 Z30	M1.5 Z30	M1.5 Z30	M1.5 Z30	M1.5 Z30
C	M1.5 Z30	M1.5 Z30	M1 Z46	M1 Z46	M1 Z46	M1 Z46	M1 Z46
D	/	/	M1 Z19	M1 Z19	M1 Z19	M1 Z16	M1 Z16
E	/	/	M1 Z19	M1 Z25	M1 Z37	M1 Z35	M1 Z44
F	M1.5 Z38	M1.5 Z19	M1 Z19	M1 Z19	M1 Z19	M1 Z16	M1 Z16
G	/	/	M1 Z14	/	/	/	/
H	/	/	M1 Z14	/	/	/	/

Note: Gear D and gear E are not needed in 1:1 and 2:1, because gear C and gear F are directly engaged.

Where M is the module of the gear, and Z is the number of teeth of the gear.

Table S2. Comparison of the volume average charge density for different cylindrical TENGs

Reference	Average power (mW)	Volume average charge density (W/m³)	Device mass (kg)	Device volume (m³)	External excitation— frequency (Hz)	External excitation— wave height (cm)
(1) WLM-TENG	0.113	0.032	/	0.0026	0.25	/
(2) WS-TENG	0.34	1.578	/	0.0033	1.5	6.8
(3) SC-TENG	0.42	1.69	/	0.0012	1	8
(4) SR-TENG	1.95	2.64	/	0.0011	1.8	/
(5) MS-TENG	6.5	3.56	/	0.0035	0.8	7
(6) MC-TENG	8.19	5.79	/	0.0042	0.8	5
(7) CS-TENG	1.95	8.48	/	0.0063	0.67	/
ER-TENG (This work)	5.54	**15.67**	3.15	0.0059	~0.8	6

References

1   J. Han, Y. Liu, Y. Feng, T. Jiang and Z. L. Wang, Adv. Energy Mater., 2023, 13, 2203219.

2   Y. Hu, H. Qiu, Q. Sun, Z. L. Wang and L. Xu, Small Methods, 2023, 7, 2300582.

3   B. Cao, P. Wang, P. Rui, X. Wei, Z. Wang, Y. Yang, X. Tu, C. Chen, Z. Wang, Z. Yang, T. Jiang, J. Cheng and Z. L. Wang, Adv. Energy Mater., 2022, 12, 2202627.

4   M. Li, Y. Lou, J. Hu, W. Cui, L. Chen, A. Yu and J. Zhai, Small, 2024, 2402009.

5   X. Wang, C. Ye, P. Chen, H. Pang, C. Wei, Y. Duan, T. Jiang and Z. L. Wang, Adv. Funct. Mater., 2023, 34, 2311196.

6   H. Yang, X. Liang, J. Kan, Z. L. Wang, T. Jiang and Z. Hong, Nano Res., 2024, 1-8.

7   H. Qiu, H. Wang, L. Xu, M. Zheng and Z. L. Wang, Energy Environ. Sci., 2023, 16, 473-483.

Table S3. Detailed cost breakdown of device parts

Component	Quantity	Unit	Unit Price (CNY)	Total Price (CNY)
Drift Barrel	1	Piece	¥16	¥16
Pendulum	1	Piece	¥25	¥25
One-way bearing	4	Piece	¥4	¥16
Ordinary bearing	28	Piece	¥1	¥28
Acrylic plate	14	300 mm*400 mm	¥2	¥28
Aluminum plate	4	100 mm*100 mm	¥4	¥16
Magnet	32	Piece	¥1	¥32
Coil spring	1	Roll	¥3	¥3
Electrode plate	8	Piece	¥2	¥16
PTFE	32	50 mm*60 mm	¥0.03	¥0.96
PA	32	50 mm*60 mm	¥0.27	¥8.64
PE	32	10 mm*52.5 mm	¥0.01	¥0.32
Total				¥189.92

Note: If it is mass-produced, the cost will be lower.

Note S1. Calculation of energy storage capacity of coil spring.

Coil spring model is represented in the diagram below. The blue curve depicts the coil spring, where the outer end remains fixed during the energy storage phase, while the inner end receives energy from the pendulum through the shaft.
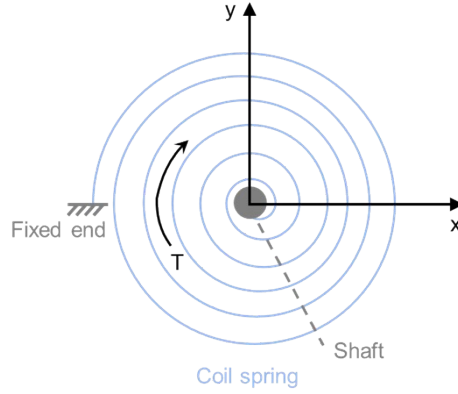
The torsional stiffness K of the coil spring with length L, width b, and thickness h, is given by:

$$K = \frac{EI}{L} = \frac{Ebh^3}{12L} \#(S1)$$

where E is the elastic modulus of the material used for the coil spring, and I is the moment of inertia of the cross-section of the coil spring. Based on the integration property, the energy stored in the coil spring, when rotated by angle $\emptyset$, is:

$$E = \frac{K\emptyset^2}{2} = \frac{Ebh^3\emptyset^2}{24L} \#(S2)$$

Due to the randomness of water waves, it is impossible to precisely measure the total energy stored in the coil spring over one cycle. However, based on simulated experimental tests, we can estimate an approximate value. E is 200 GPa, b is 14 mm, h is 0.14 mm, $\emptyset$ is approximately 4500°, L is 3250 mm. Therefore, the energy storage capacity of coil spring per cycle is about 1994.68 mJ.

Note S2. Influence of centrifugal speed limiter on the transmission efficiency of the device.

To install the speed limiter, additional Gear H and G are introduced to the gear set. Assuming the transmission efficiency equals 1 without the limiter, the transmission efficiency η is determined by the gear meshing efficiency η_g, bearing friction loss efficiency η_b, and loss efficiencies caused by the centrifugal speed limiter η_o.

$$\eta = \eta_g \cdot \eta_b \cdot \eta_o \#(S3)$$

Since gear H and gear G are both straight, η_g can be calculated by

$$\eta_g = 1 - \frac{2.6\mu}{cos\beta_b}\left(\frac{1}{Z_1} + \frac{1}{Z_2}\right)\#(S4)$$

where μ is the inter-tooth sliding friction factor, which equals 0.05 due to low tooth roughness. β_b is the angle of inclination of the teeth on the base circle, which is 20°. Z_1 is 19 and Z_2 is 14. Thus, η_g can be calculated as 0.9917. For the bearing friction loss efficiency η_b, its empirical value is 0.995. The loss efficiency η_o caused by the centrifugal speed limiter can be calculated analogously to the non-liquid friction centripetal plain bearing friction loss efficiency. This theoretical calculation is very cumbersome, but it generally ranges from 0.92 to 0.96. We choose 0.94 because the three elastic flaps are not completely in contact with the stopper ring. Up to this point, the transmission efficiency η is 0.9229. Therefore, the addition of the centrifugal speed limiter reduces the energy transmission efficiency to 92% of that without the limiter. These are theoretical calculations, but from a qualitative and empirical perspective, the centrifugal speed limiter stops rotating under a tiny external force, indicating its low load-carrying capacity. In contrast, the magnet startup plate can drive the stacked TENGs to work. Consequently, most of the energy input to Gear A is still supplied to the startup plate, and the centrifugal speed limiter has a minimal effect on the device's overall efficiency.

Note S3. Durability analysis of the ER-TENG's mechanical structure.

To begin, let's discuss the bearing lifespan. Since each bearing is connected to a different gear, their lifespans vary. Therefore, we only need to calculate the lifespan of the bearing with the shortest life expectancy. In Fig. 2c, it is clear that the bearing corresponding to gear A experiences the largest equivalent dynamic load (P) due to the progressive transmission losses and torque levels. Given that bearing lifespan is a discrete variable, it should be calculated in relation to a specific reliability level. The relationship between bearing reliability and lifespan can be expressed by the following formula:

$$\frac{\ln R}{\ln 0.9} = \left(\frac{L_{100-R}}{L_{10}}\right)^p \#(S5)$$

where R represents the reliability of the bearing, L_{100-R} is the lifespan of the bearing when the reliability is R, and L_{10} with a value of 10^6, is the basic rated life of the bearing, measured in revolutions. The exponent p is the life dispersion factor of the bearing, and for this experiment, p is 10/9. To ensure higher reliability of the mechanical device, we choose a bearing with an extremely high reliability of R=99%. Therefore, when calculating the bearing lifespan, the reliability-adjusted life factor L_{10m} replaces L_{10}, and L_{10m} is calculated as $L_{10m}=0.189{\times}L_{10}$. The relationship between bearing load and lifespan for rolling bearings is given by:

$$P^\varepsilon L_{10} = constant\#(S6)$$

where ε is the life exponent, which is set to 3 for our bearings. The basic rated load that the bearing can withstand for a lifespan of 10^6 revolutions is referred to as the basic dynamic load rating C (with a value of 496 N for this bearing). By introducing the temperature factor f_t (set to 1 at normal temperature) and the load factor f_p (set to 1.2), substituting into equation (S6) gives:

$$L_{10} = 10^6 \left(\frac{f_t C}{f_p P}\right)^\varepsilon \#(S7)$$

The spur gears, which do not bear axial forces, are used. So the equivalent dynamic load on the bearing P equals the radial force F_R, measuring 1.942 N. Ultimately, we figure out that $L_1 = 2.2 * 10^{11}$ revolutions, which fully meets the operational requirements.

Next, let's discuss the durability of the gears. The primary failure modes for gears are surface fatigue

pitting and root bending fatigue fracture. Therefore, we need to calculate the contact fatigue strength of the gear surface and the bending fatigue strength of the gear root. Taking gear B as an example, the surface contact fatigue strength σ_H is calculated based on Hertz contact stress theory and can be expressed by the following formula:

$$\sigma_H = Z_E Z_H Z_\varepsilon \sqrt{\frac{KF_t}{bd_1} \frac{u+1}{u}} \#(S8)$$

$$Z_E = \sqrt{\frac{1}{\pi\left(\frac{1-\mu_1^2}{E_1} + \frac{1-\mu_2^2}{E_2}\right)}}, Z_H = \sqrt{\frac{2}{\cos\alpha\sin\alpha}}, Z_\varepsilon = \sqrt{\frac{(4-\varepsilon_\alpha)}{3}}\#(S9)$$

where K is the load factor, set to 1.2, F_t is the tangential force on the gear, calculated to be 1.82 N, b is the working width of the gear tooth, set to 3 mm, d_1 is the pitch diameter of the gear, set to 57 mm, u is the gear ratio between gear B and gear A, set to 0.79, the Poisson's ratios μ_1 and μ_2 are both 0.3, the elastic moduli E_1 and E_2 are both 69 GPa, the pressure angle α is 20° and the contact ratio ε_α is calculated to be 1.69. Substituting these values into equation (S8) gives σ_H=40.905 MPa. The allowable contact stress $[\sigma_H]$ for the material we are using, 6061 aluminum alloy, is approximately 93 MPa, which meets the experimental requirements.

For the bending fatigue strength of the gear root, we consider the stress concentration effects at the root fillet and the impact of other stresses besides bending stress on the root stress. The verification formula is:

$$\sigma_F = \frac{KF_t}{bm}Y_{Fa}Y_{Sa}Y_\varepsilon \leq [\sigma_F]\#(S10)$$

$$Y_\varepsilon = 0.25 + \frac{0.75}{\varepsilon_\alpha}\#(S11)$$

where σ_F represents the calculated bending stress. The gear modulus m is 1.5, the tooth form factor Y_{Fa} is 2.45, and the stress correction factor Y_{Sa} is 1.65, both obtained from charts. The contact ratio factor Y_ε is calculated to be 0.694. Substituting these values into Equation 6 gives σ_F=1.362 MPa. The

allowable bending stress $[\sigma_F]$ for the aluminum alloy we are using is approximately 120 MPa, which also meets the experimental requirements.

In conclusion, the mechanical components of the device exhibit excellent durability, fully capable of meeting the long-term operational demands of power generation.
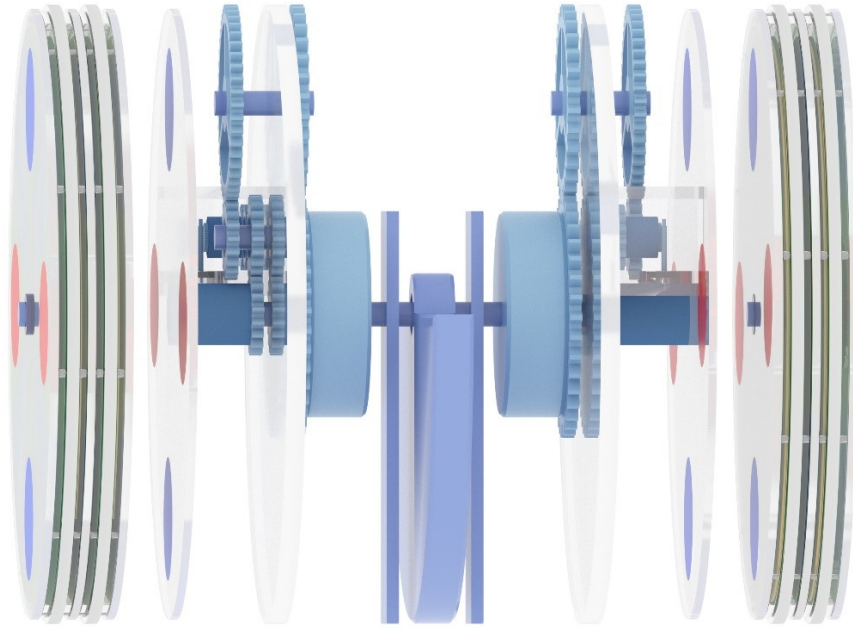
Fig. S1. Components of ER-TENG, which are symmetrically positioned around a central pendulum.
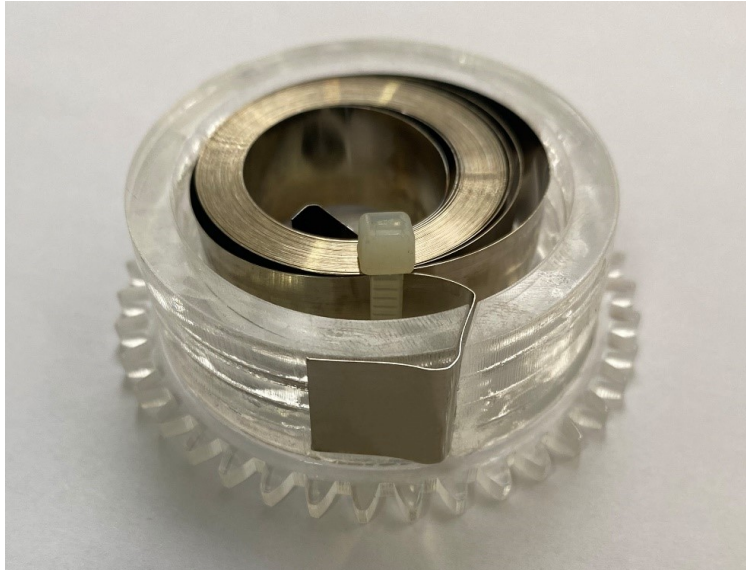
Fig. S2. Photograph of the outer end of the spring embedded in the container shell (The shell is made of acrylic just for easy viewing).

a

b **Free rolling**

Elastic sheet

Unlocked state

c **Frictional resistance**

Locked state
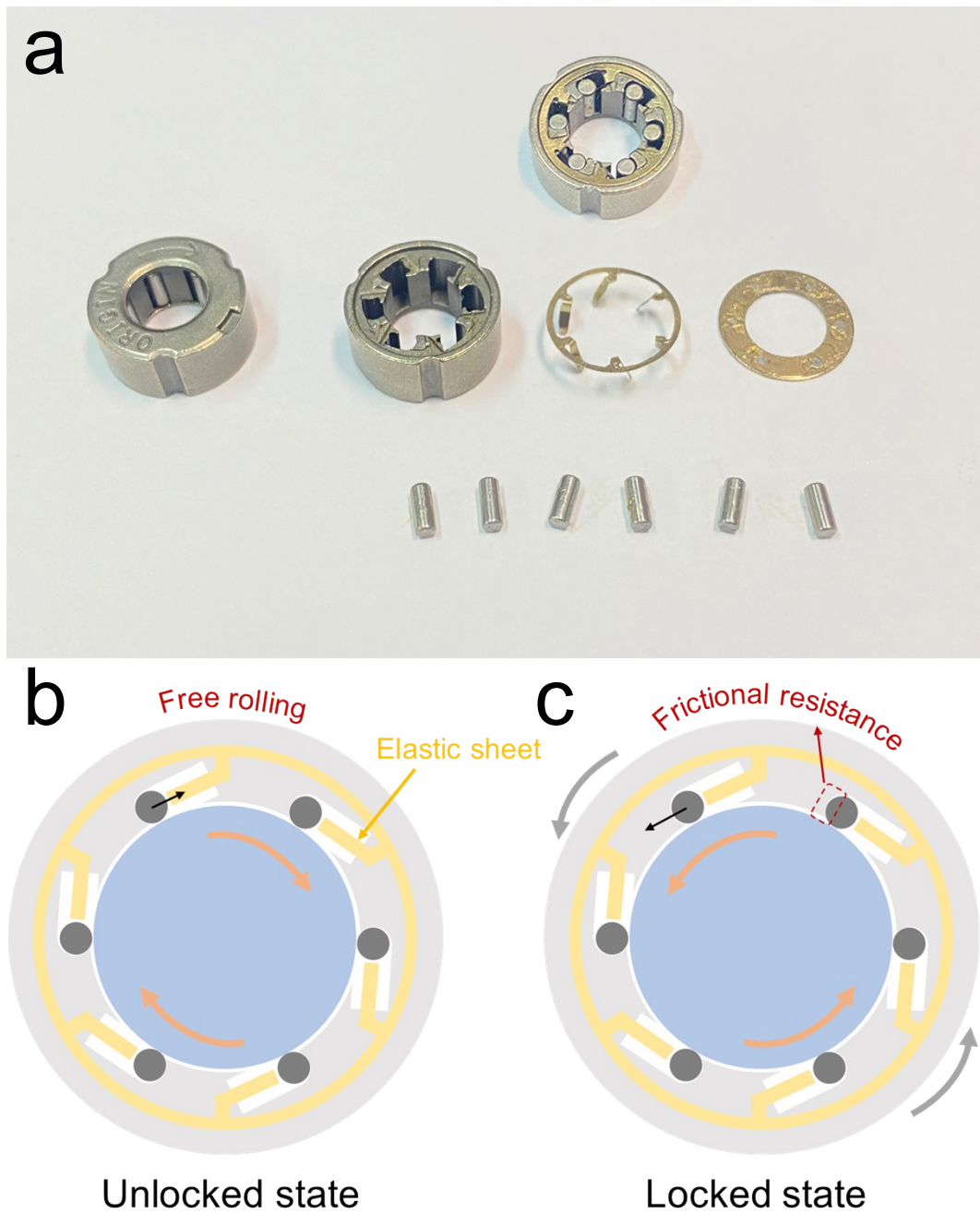
Fig. S3. (a) Photograph of a one-way bearing, including the overall appearance, interior structure, and all parts of the bearing. (b-c) Working process of the one-way bearing.

$Ep = 0$

Δh

$Ep = mg\Delta h$

$Ep = 0$

Barycenter
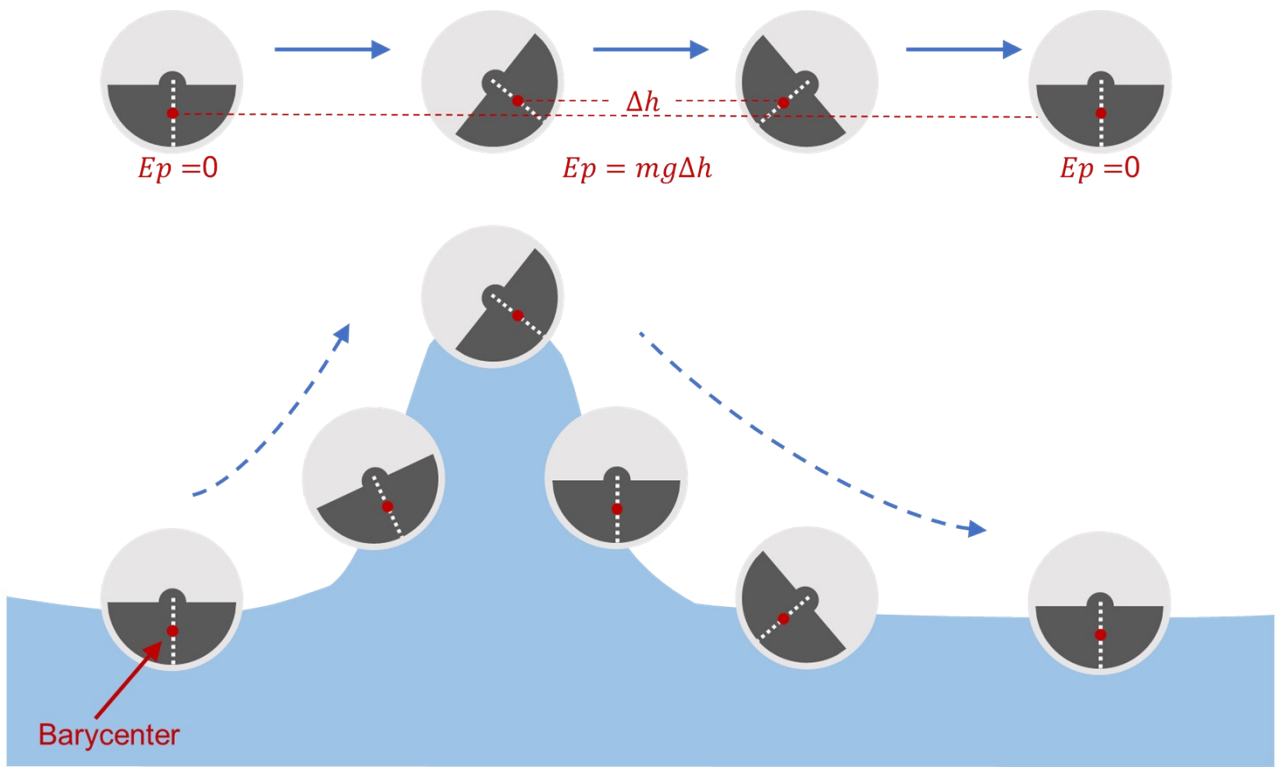
Fig. S4. Energy conversion process from wave to the pendulum.
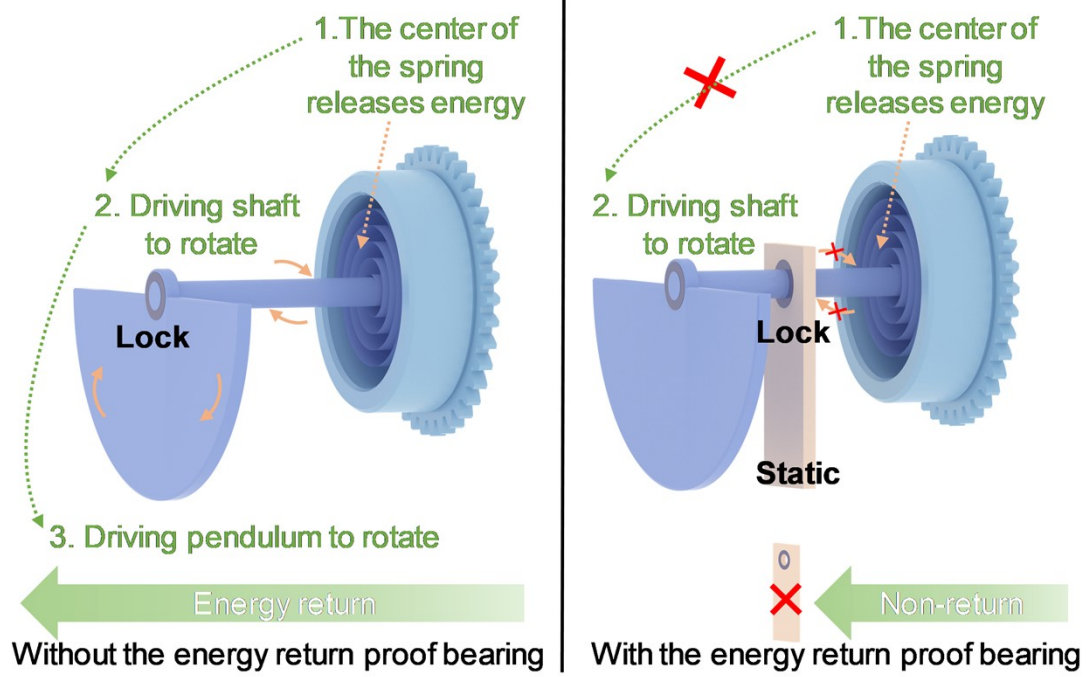
Fig. S5. Working principle of the energy return proof bearing.

$y = a_{w\,i\,t\,ho} + b_{w\,iu\,t\,ho} * x_u$
$a_{w\,i\,t\,ho} = 6.50251 \pm 0.01577$
$b_{w\,i\,t\,ho} = 0.0249 \pm 5.25129E-4$
$R_{w\,i\,t\,ho} = 0.20361$

$y = a_{w\,i\,t} + b_{w}i * x\,t$
$a_{w\,i\,t} = 10.13213 \pm 2.70586E-4$
$b_{w\,i\,t} = 0.02728 \pm 9.37325E-6$
$R_{w\,i\,t} = 0.99706$
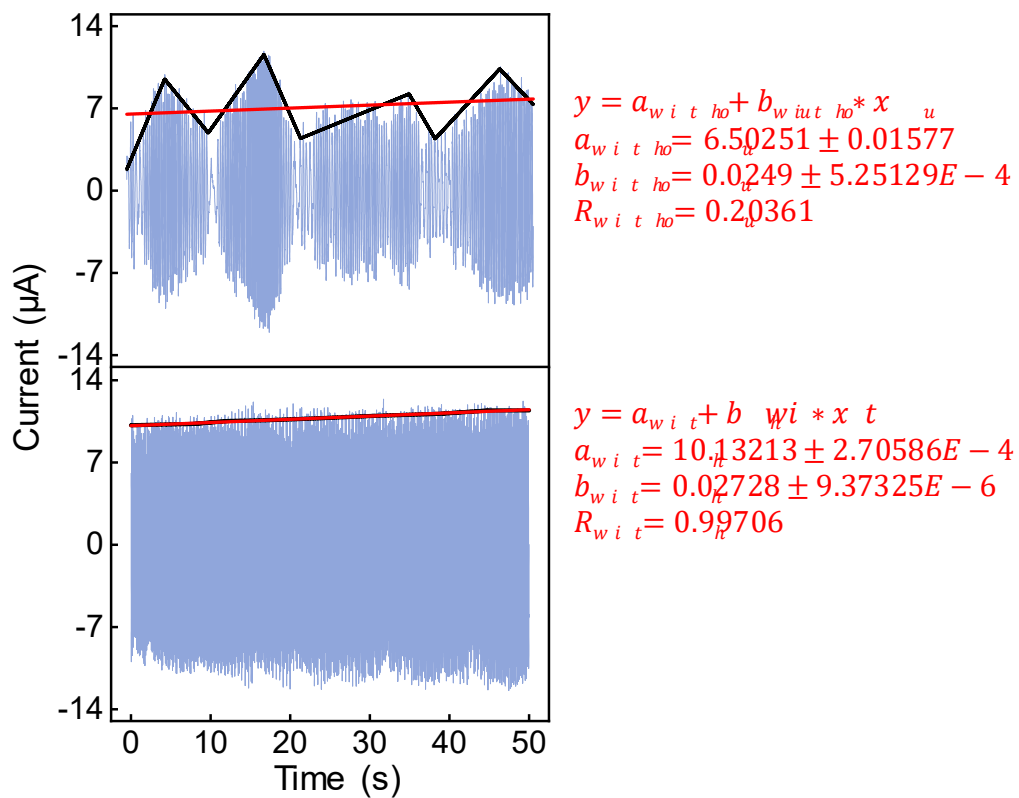
Fig. S6. Peak linear fitting graphs of two output curves.
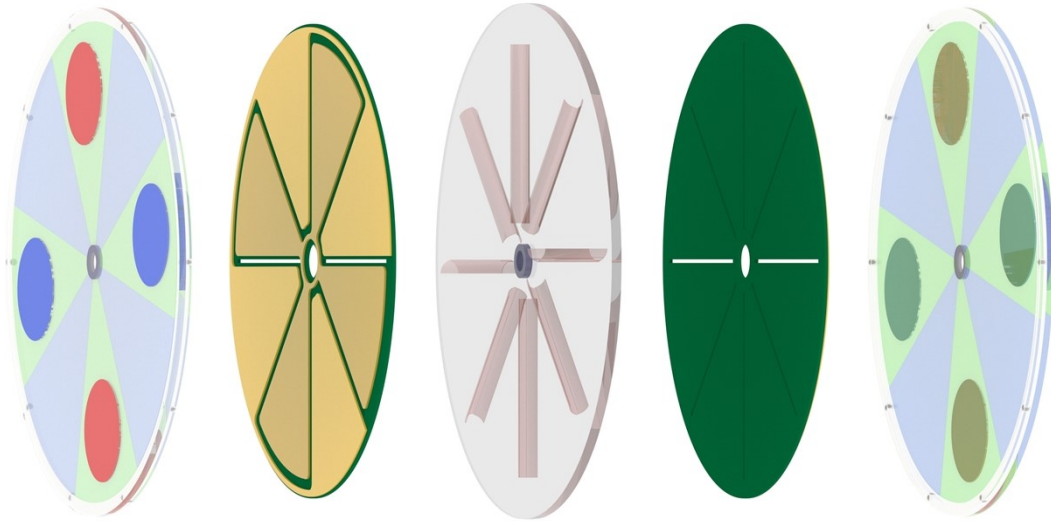
Fig. S7. Schematic diagram of each layer for the test device.
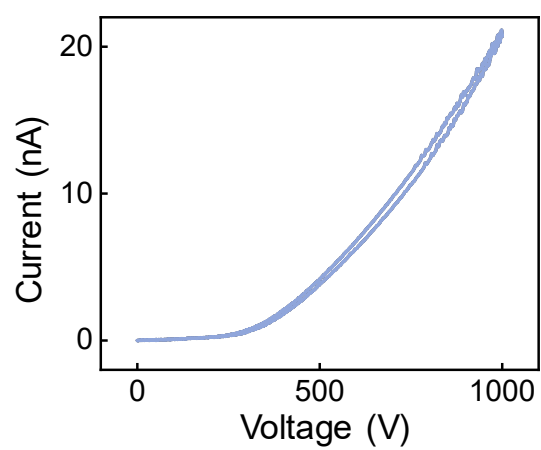
Fig. S8. Charge dissipation curve of PA film.
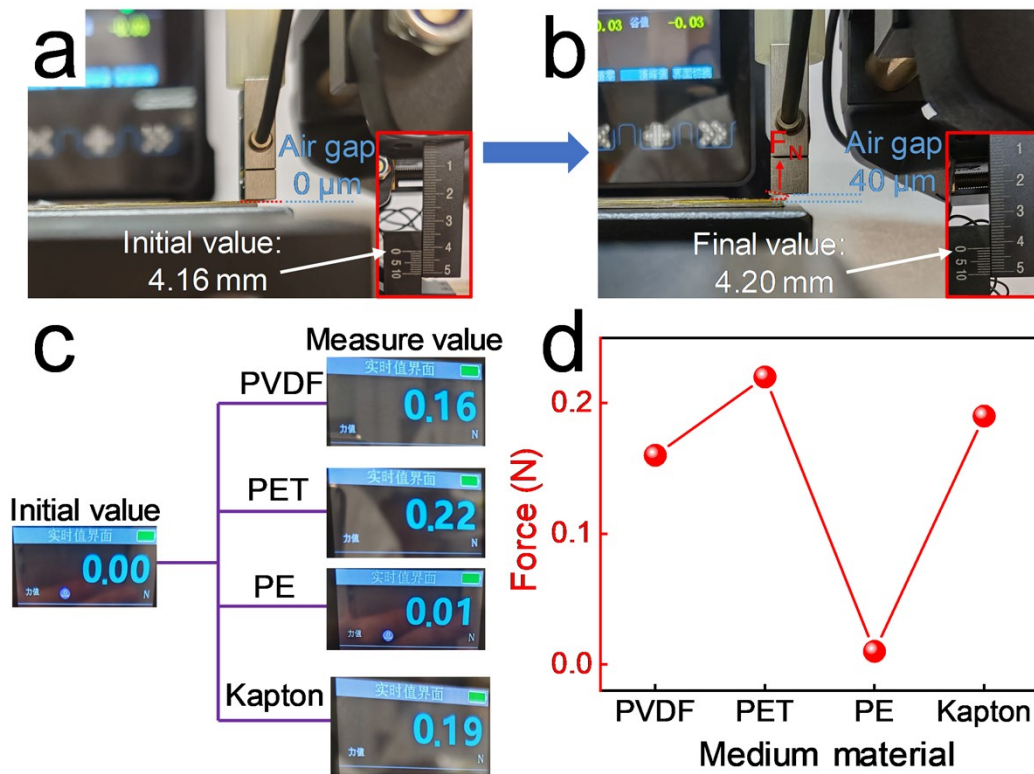
Fig. S9. Measured interaction force between medium materials and the rotor. (a-b) Digital photo of the initial and final state, indicating the height of the force sensor at this moment. (c-d) Measured results of different medium materials.
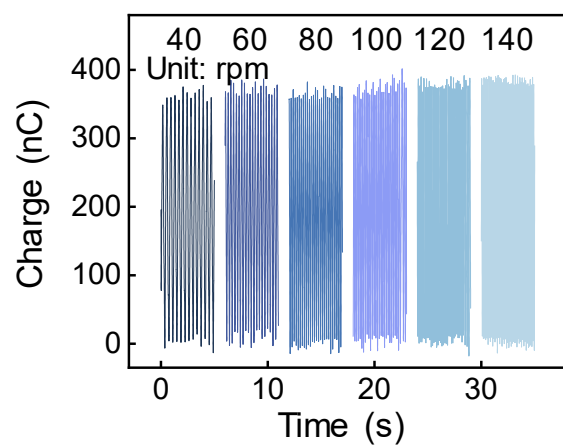
Fig. S10. Transferred charge curves of TENG from 40 to 140 rpm.
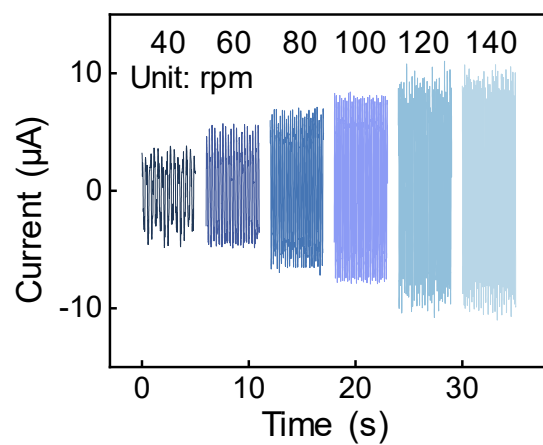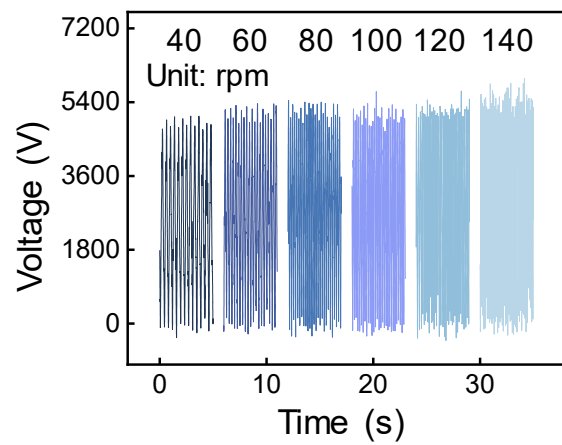
Fig. S11. Short-circuit current curves of TENG from 40 to 140 rpm.

Fig. S12. Open-circuit voltage curves of TENG from 40 to 140 rpm.
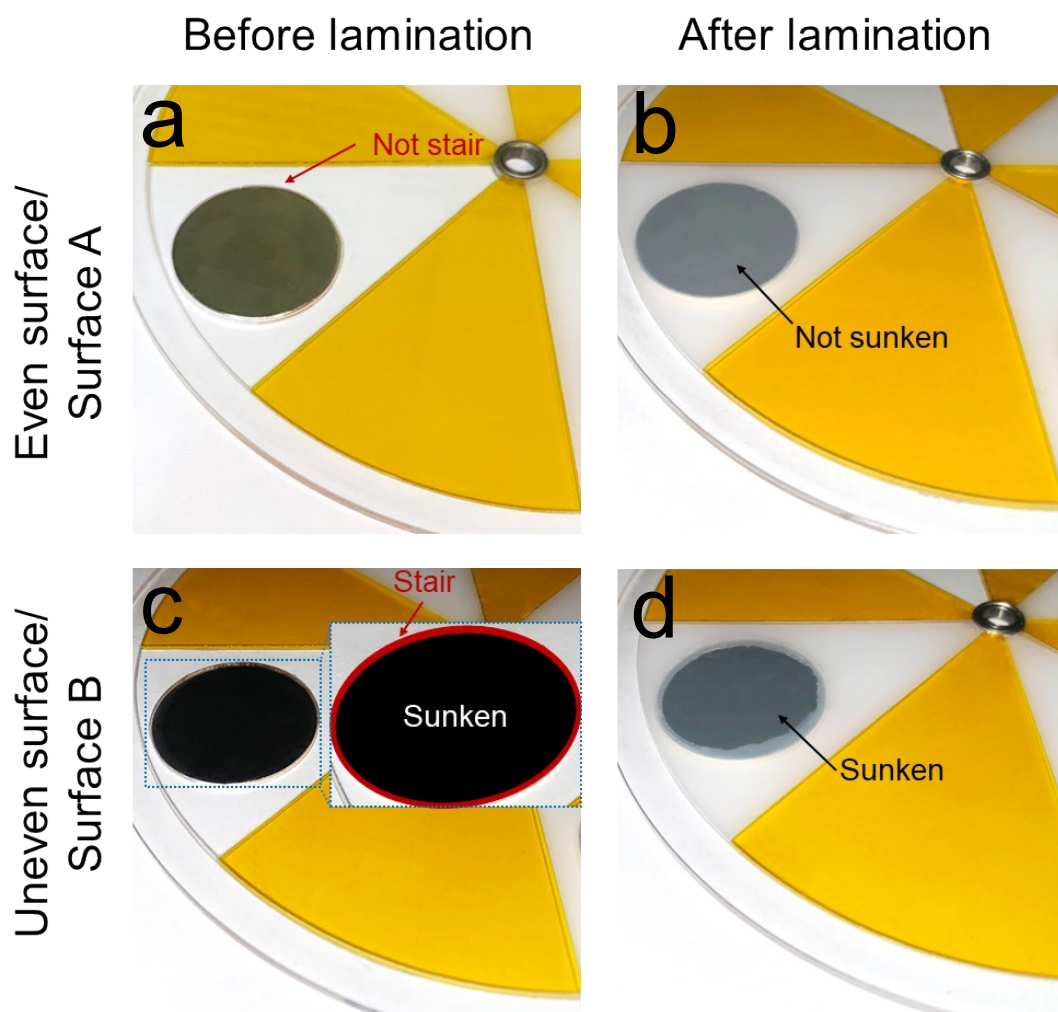
Fig. S13. Digital photos of magnets embedded in the acrylic plate. (a-b) Digital photos of the even surface before and after attaching the PTFE. (c-d) Digital photos of the uneven surface before and after attaching the PTFE.
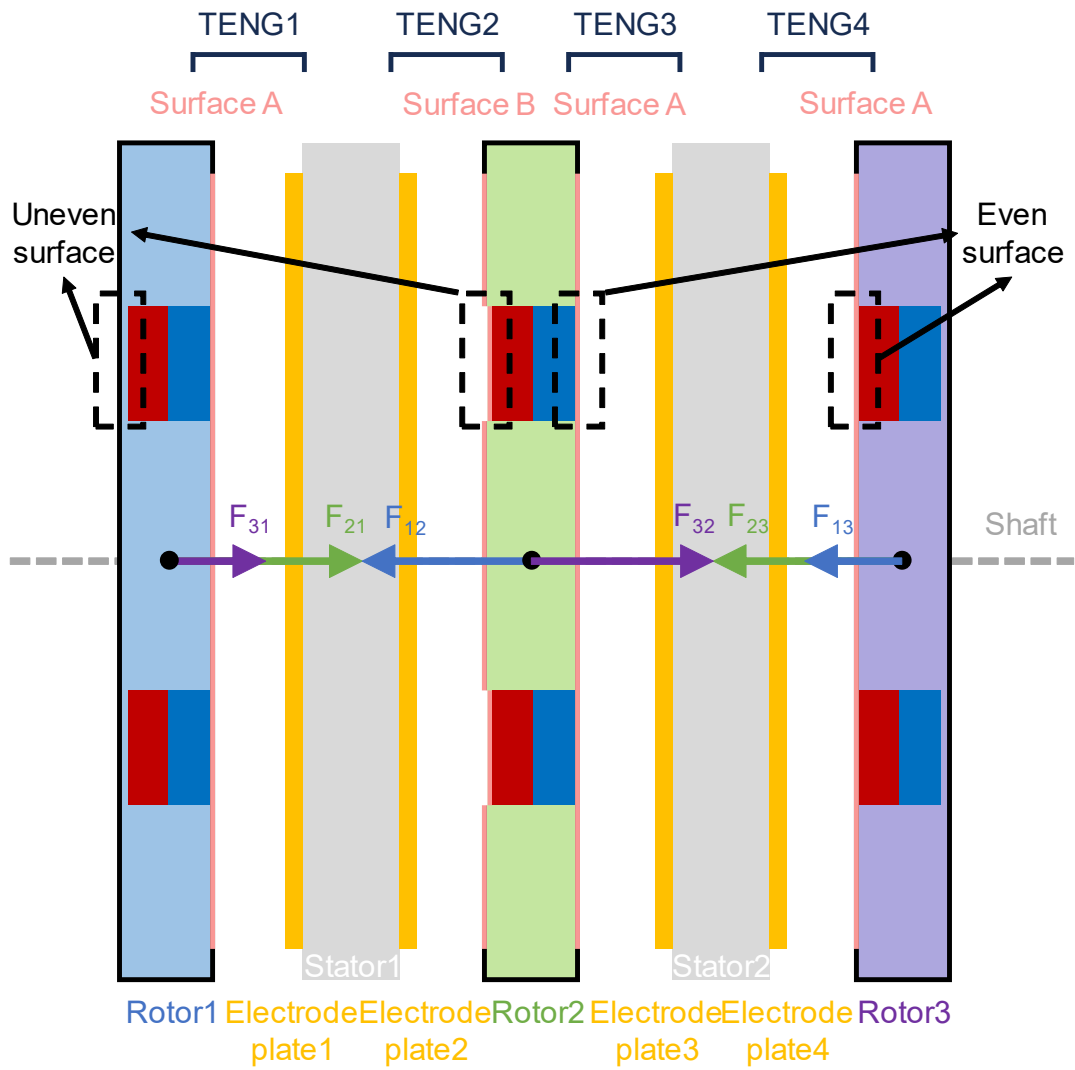
Fig. S14. Schematic diagram of the distribution of surface A and surface B, and the force analysis between the three rotor layers.
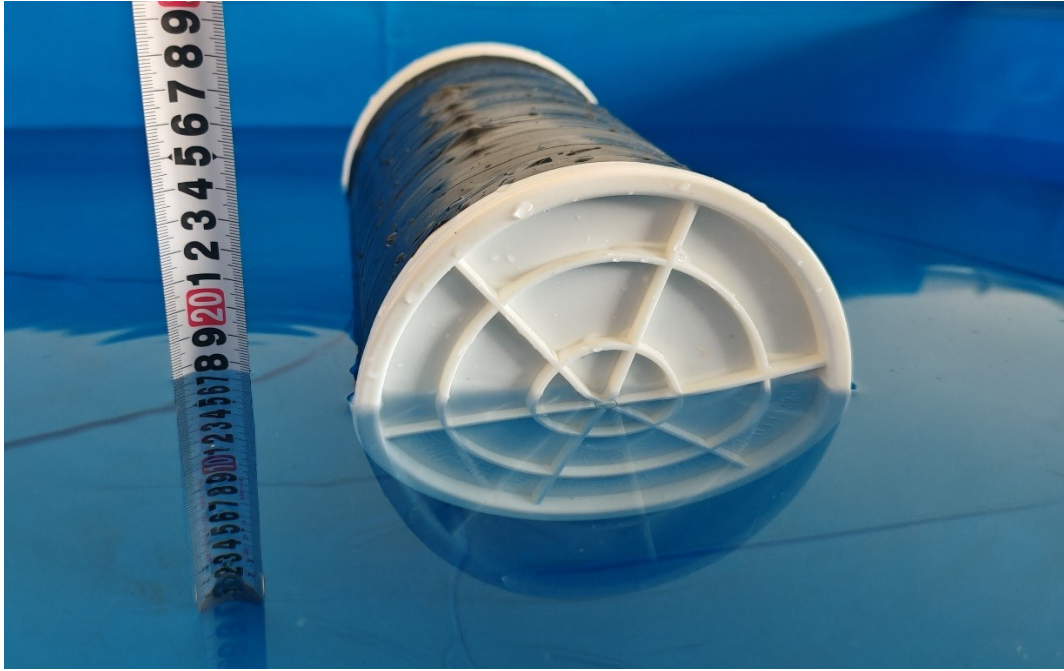
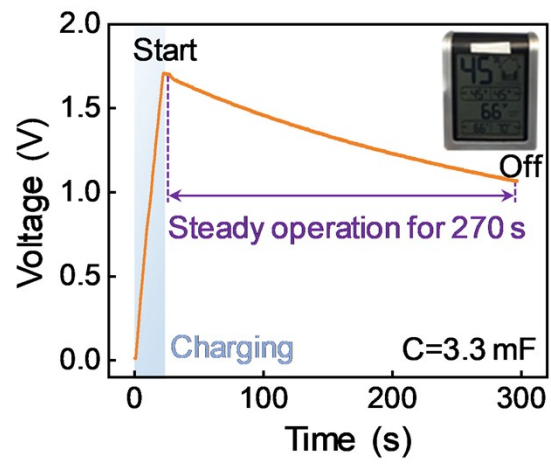**Fig. S15.** Photograph of the ER-TENG floating on the water.

Fig. S16. Voltage curve of the thermohygrometer driven by ER-TENG with PMC. Inset is the work state.
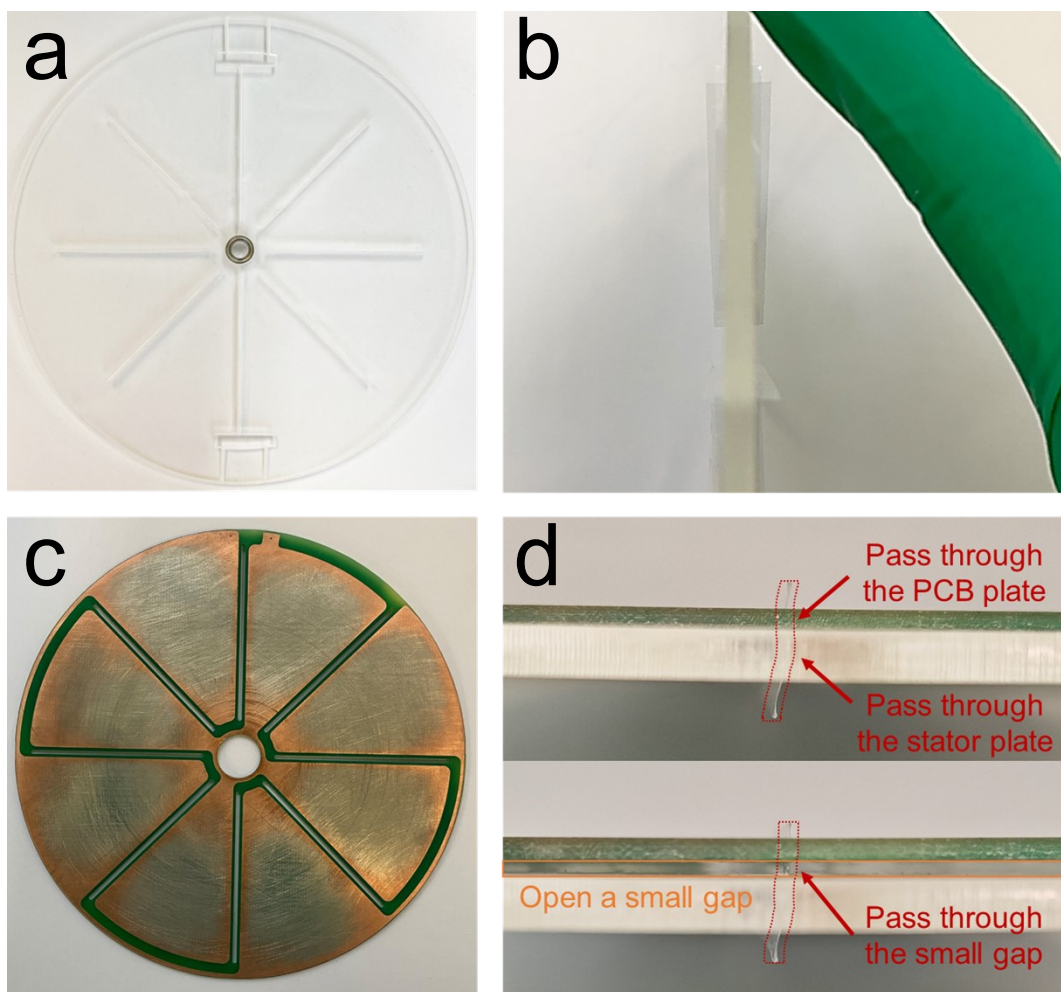
Fig. S17. (a) Top and (b) side view of the stator fixing medium materials. (c) Top view of electrode plate, the gap is clearly visible. (d) Side view of the PE passing through the gap of the electrode plate.
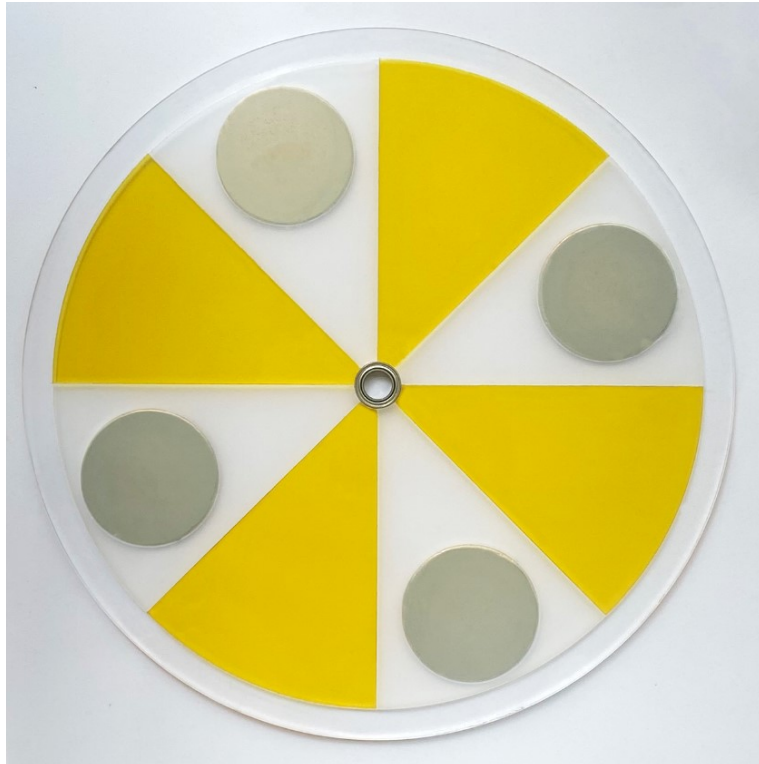
Fig. S18. A photograph of the rotor, where the yellow area represents the 25 μm PA film and the milky white area represents the 10 μm PTFE film.
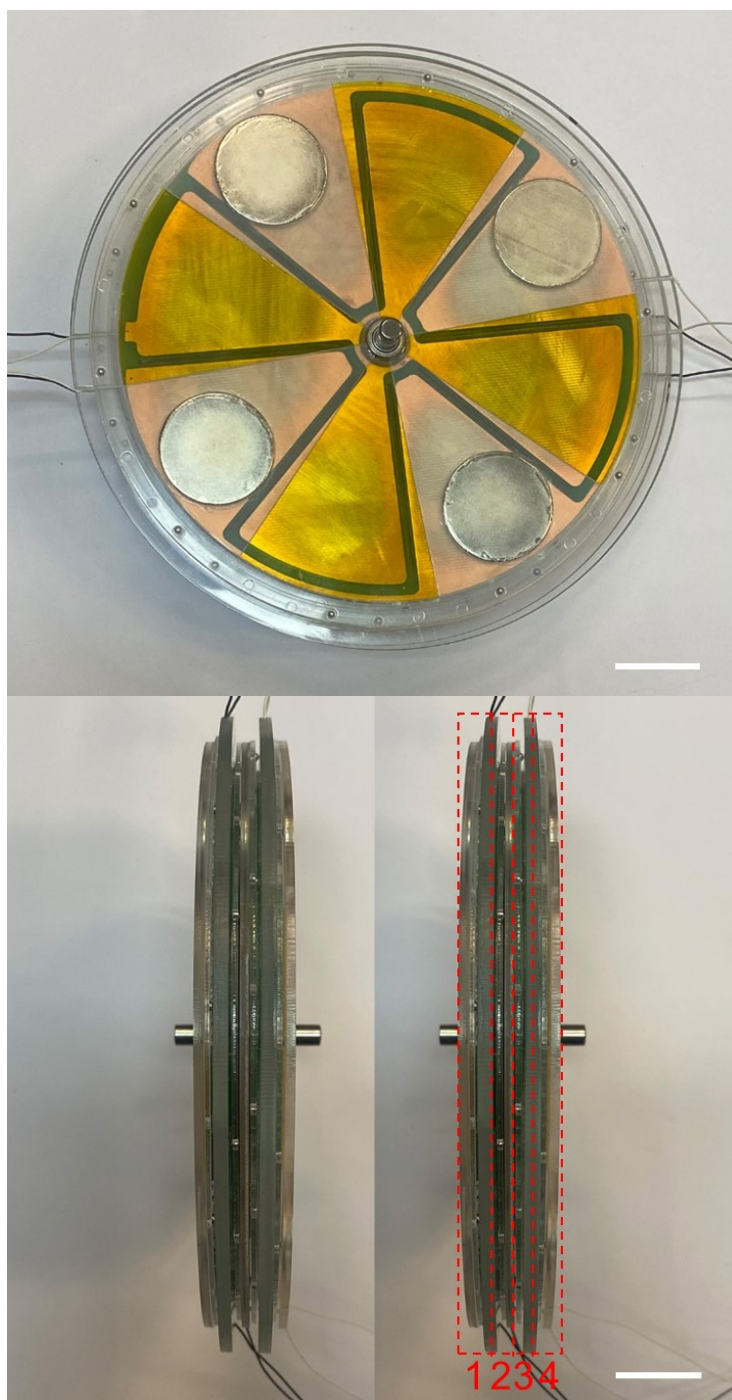
Fig. S19. Top and side view of the stacked TENG. Scale bar is 2 cm.

Fig. S20. Photograph of the mass (kg) of ER-TENG.